

Parallel Structured/Unstructured Simulation Of Missile Dynamic Flowfields*

A. Hosangadi, P.A. Cavallo, and S. Arunajatesan
Combustion Research and Flow Technology, Inc.
174 North Main Street, P.O. Box 1150
Dublin, PA 18917
Phone: 215/249-9780 Fax: 215/249-9796
E-mail: hosangad@craft-tech.com

and

Dr. Kevin Kennedy
Army Aviation and Missile Command
Redstone Arsenal, AL

1.0 INTRODUCTION

This paper provides an overview of accomplishments achieved during the course of an HPC Challenge Grant focused on the simulation of missile dynamic flowfields. The technical approach entails utilization of structured grid and multi-element unstructured grid parallelized Navier-Stokes codes which have been operational on varied HPC computers for the past several years. Specific problems addressed are:

- (1) the analysis of dynamic multi-body flows using unstructured numerics with unique grid control and automated remeshing procedures – applications to missile submunition dispense and shroud deployment are described;
- (2) large eddy simulation for control of aeroacoustic flowfields using higher-order structured numerics – applications to control of pressure oscillations in cavities and to analysis/control of vibrations are described; and,
- (3) use of multi-phase gas/liquid numerics to analyze the interactions (deformation and breakup) of chemical agents released in post-hit threat missile scenarios.

The CRAFT CFD structured grid and CRUNCH CFD unstructured grid Navier-Stokes codes were utilized in these calculations whose overall features are summarized in Tables I and II below.

Table I. Relevant Features of CRAFT Navier-Stokes Code.

<i>NUMERICS/ PARALLEL PROCESSING</i>	<ul style="list-style-type: none">• 1D/2D/AXI/3D Finite-Volume Discretization• Implicit, ADI and L/U, Higher-Order Upwind (Roe/TVD) Formulation• Fully Implicit Source Terms/Boundary Conditions• PNS Spatial Marching Capability• Domain-Decomposition Parallel Architecture with MPI• Shared Memory Parallelism• Preconditioning Extensions
<i>GRID FEATURES</i>	<ul style="list-style-type: none">• Grid Dynamics to Account for Moving Boundaries• Grid Patching/Blanking for Complex Geometries• Solution-Adaptive Gridding and Grid Embedding• Noncontiguous Grid Interfacing with Flux Preservation Across Domains
<i>THERMO- CHEMISTRY</i>	<ul style="list-style-type: none">• Multi-Component Real Gas Mixtures• Finite-Rate Chemistry/Arbitrary Number of Species and Reactions• Fully Implicit Source Term Linearization
<i>MULTIPHASE FLOW</i>	<ul style="list-style-type: none">• Nonequilibrium Particle/Droplet Solvers (Eulerian and Lagrangian Formulations)
<i>TURBULENCE</i>	<ul style="list-style-type: none">• k-epsilon /EASM Formulations with Compressibility/Vortical Upgrades• LES Subgrid Scale Models – Algebraic and One-equation

*Presented at The DOD HPCMP User's Group Conference 2002, University of Texas, Austin, TX, June 10-13, 2002.
UGC 2002

Table II. Relevant Features of CRUNCH Navier-Stokes Code.

<i>NUMERICS</i>	<ul style="list-style-type: none"> • Finite-Volume Roe/TVD Flux Construction, Vertex Storage
<i>INTEGRATION</i>	<ul style="list-style-type: none"> • Explicit Four-Step Runge-Kutta, Implicit GMRES, Gauss-Seidel
<i>GRID ELEMENTS</i>	<ul style="list-style-type: none"> • Tetrahedral, Hexahedral, Prismatic, Pyramid
<i>PARALLEL PROCESSING CAPABILITIES</i>	<ul style="list-style-type: none"> • Domain Decomposition MPI, Independent Grids with Noncontiguous Interfacing, Automated Load Balancing
<i>DYNAMIC GRID CAPABILITIES</i>	<ul style="list-style-type: none"> • Node Movement Solver (Implicit Elasticity Approach), Automated Embedding, Sliding Interfaces
<i>GRID ADAPTION</i>	<ul style="list-style-type: none"> • Variable Element Grid Refinement using Delaunay and cell subdivision Procedures, Automated Load Balancing of Adapted Grid
<i>THERMOCHEMISTRY</i>	<ul style="list-style-type: none"> • Multi-component Real Gas Mixtures, Finite-Rate Kinetics
<i>TURBULENCE RANS/LES</i>	<ul style="list-style-type: none"> • k-epsilon /EASM Formulations with Compressibility/Vortical Upgrades • LES Subgrid Scale Models – Algebraic and One-equation • Algebraic (Smagorinsky) and Single Equation (k) SGS Models
<i>MULTIPHASE FLOW</i>	<ul style="list-style-type: none"> • Nonequilibrium Particle/Droplet Solvers (Eulerian and Lagrangian Formulations)

2.0 DYNAMIC MULTI-BODY SIMULATIONS

Computational simulations of moving body problems present significant challenges to current CFD techniques. Two fundamental difficulties include the need to move the computational mesh, and provide adequate resolution to capture an evolving, transient flowfield. Overset mesh Chimera techniques have traditionally been employed to simulate separation scenarios. While these methods readily accommodate grid motion, they also require considerable experience of an expert user to operate. With flow features changing dramatically, the Chimera approach does not address the issue of providing appropriate grid resolution “on the fly.” Furthermore, there is great expense associated with the need to frequently update the inter-grid interpolation stencils as the meshes slide through each other.

Unstructured grid methods offer distinct advantages over Chimera schemes in that flow structures may be readily resolved by locally splitting or embedding cells, and setup times are substantially reduced. The primary challenge in applying an unstructured grid approach to multi-body flows lies in maintaining a valid, well-shaped mesh as the bodies move. Our research focuses on the use of grid movement procedures combined with periodic mesh adaptation based on geometric criteria. Substantial changes in the motion of bodies have been demonstrated with this unified, single-grid approach. Furthermore, the multi-element unstructured grid framework offers superb grid generation flexibility and readily permits solution adaptation to simultaneously provide enhanced resolution for the changing flow structures inherent in separation problems. This section describes the use of the unstructured Navier-Stokes solver, CRUNCH CFD [1], and a mesh adaptation package, CRISP CFD [2,3], in multi-body flowfield applications.

Mesh movement in CRUNCH CFD is accomplished in parallel through use of a solid body stress analogy [4]. Given a change in the boundary mesh, such as that associated with the motion of bodies, the interior nodes of the grid are redistributed by means of a generalized node movement solver based on equations of elasticity. This node movement scheme has proven to be much more robust than commonly used spring analogy techniques, as representing the full stress tensor allows mesh deformations to be propagated farther into the field, particularly for torsional stresses.

Figure 1 illustrates an example of grid motion on a multi-element tet/prism mesh. In this sequence of images, a generic store is translating downward and downstream of a weapons bay cavity. The viscous prism cells adjacent to the store move with the body, and the surrounding tetrahedra stretch and compress to accommodate the motion. Mesh modifications to alleviate the resulting distortion are limited to the tetrahedral portion of the domain.

Mesh movement alone cannot tolerate the entire trajectory of a store. For large degrees of motion the unstructured mesh will eventually become so distorted that the resulting poor element quality will affect the computed flowfield, or worse, inverted elements will form terminating the

simulation. A means of detecting and monitoring these mesh deformations is needed to inform the refinement and coarsening modules where and how to modify the grid.

A mesh deformation matrix concept [5] is employed to automatically detect distorted regions of the grid in need of modification. The analysis examines the transformation of a tetrahedral element from its initial state at time t_0 to its current shape at time t_1 . This transformation can be represented by a deformation matrix that can be further decomposed into two matrices that represent dilatation and rigid body rotation. The eigenvalues of this deformation matrix represent the dilatation of the tetrahedron in each of three principal directions. In the limit, eigenvalues of one correspond to an undeformed element, while an eigenvalue of zero indicates a cell that has collapsed to zero volume. The ratio of minimum to maximum eigenvalue forms a condition number, bounded between 0 and 1, that indicates the extent of deformation from the initial state at t_0 .

This condition number is then used to drive mesh adaptation. Figure 2 illustrates an example of how the condition number is used to isolate regions of a deformed viscous grid in need of correction. The black isosurface denotes a condition number of 0.9, above which we consider the elements to be undeformed. Mesh coarsening is then carried out by prescribing a larger point spacing, using the condition number. Note that if the element is undeformed, this condition number is unity and the value of the point spacing is unchanged. Conversely, for severely distorted cells the condition number decreases and the spacing is increased so that the region is sufficiently coarsened, removing poor cells. After the coarsening stage, a Delaunay refinement procedure restores proper point spacing suitable to the current state of the solution and/or the length scales of the original grid. This refinement stage recovers the original point spacing and mesh quality, and is the logical point for solution-based adaptation. In the current example, the original point spacing has been restored after each coarsening phase. Note how the deformation above and below the store is effectively detected and corrected using these methods.

Using this approach, appreciable motions may be accommodated without introducing severe mesh distortion. One such example is that of missile nosecone shroud dispense into a hypersonic freestream. Prior to initiating final maneuvers interceptor missiles deploy nosecone shields, which protect sensitive sensor regions throughout much of the flight. Figure 3 gives an overview of the problem under consideration. This study represented an important step toward the use of adaptive unstructured methods for providing dynamic mesh correction and solution refinement in transient separation analysis [6]. Figure 4 depicts Mach number contours and tetrahedral meshes on the body surfaces and symmetry plane during the dispense. Note the dramatic changes in shock structure present as the opening shroud petals create a forward-facing cavity, until eventually each body lies outside the influence region of the others.

Since the modified grid will have been refined in certain areas and possibly coarsened in others, the mesh should be decomposed into a new set of load-balanced partitions for optimal parallel solution processing. This issue is most important for transient applications, where a load balancing that is transparent to the user is desirable. The present procedure requires some monitoring by the user, with load redistribution as a “man-in-the-loop” event. Automated load balancing for transient problems is currently being explored using the ParMETIS [7] mesh partitioning library.

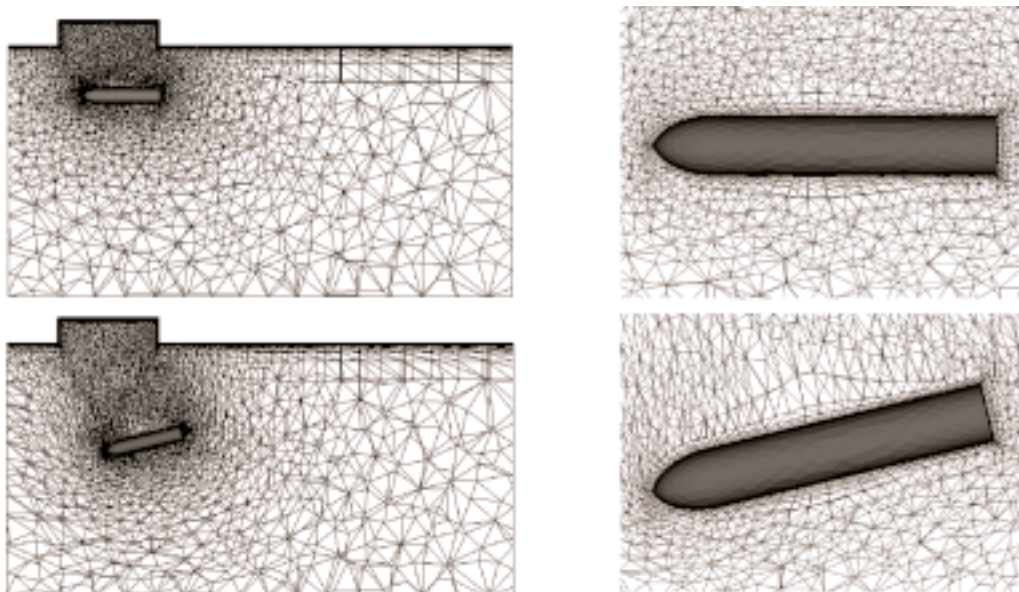


Fig. 1. Viscous grid motion for prescribed store trajectory.

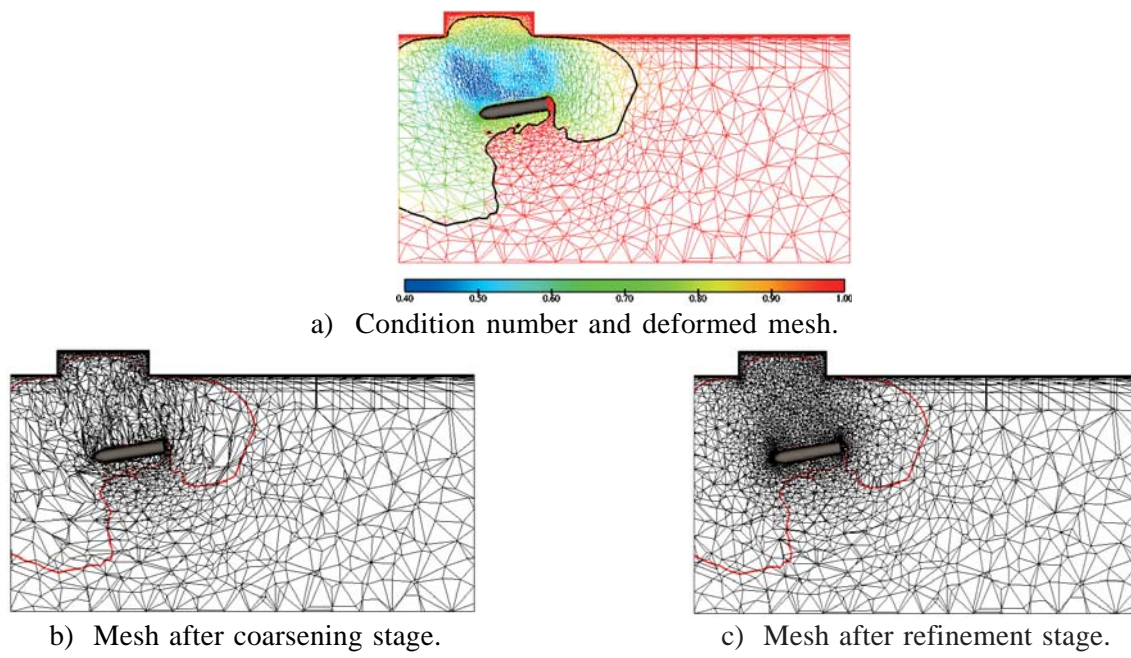


Fig. 2. Use of matrix condition number in dynamic mesh adaptation.

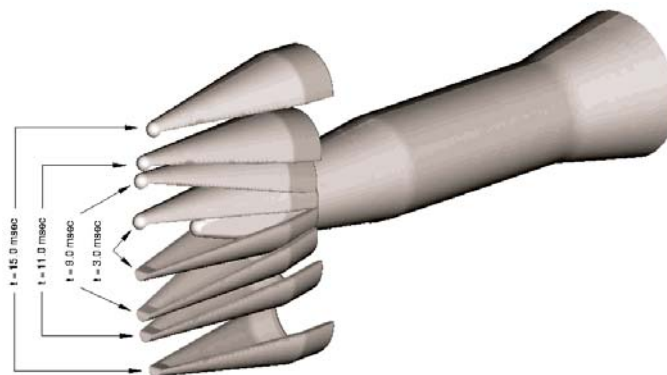


Fig. 3. Overview of AIT shroud deployment.

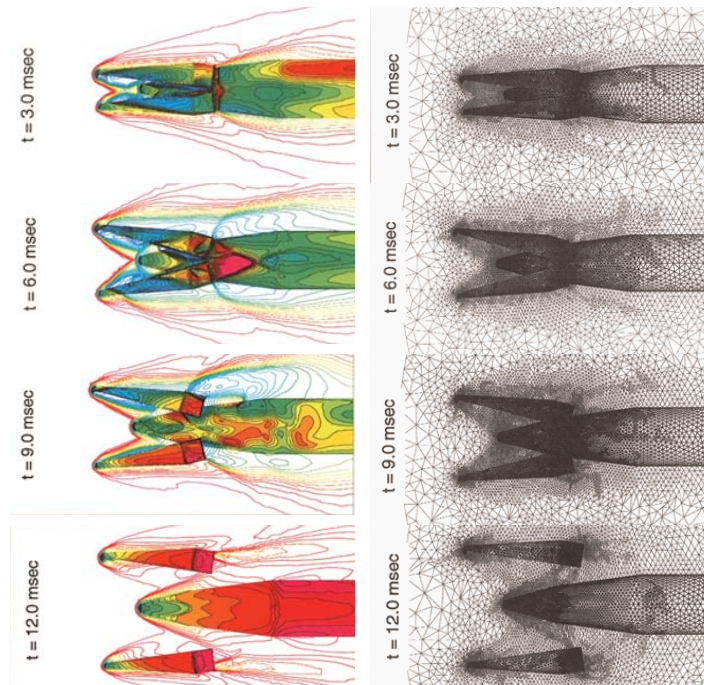


Fig. 4. Shroud separation, Mach number contours and computational meshes.

3.0 LARGE EDDY SIMULATIONS FOR CONTROL OF AEROACOUSTIC FLOW FIELDS

A large fraction of the HPCC time allotted to CRAFT Tech has been used in computing aeroacoustic flow fields with the aim of developing control strategies for these flows. Some of the flows studied include high speed flow over cavities, lateral divert jet interaction flow fields, high speed boundary layers and impinging jets. The main issues addressed the past year concern the use of appropriate numerics for LES of high speed flows, analysis of control mechanisms and development of lower dimensional models using results of these simulations. In this section we describe these studies.

3.1 Numerics for LES of High Speed Flows

For high speed applications where shock waves are present, higher order numerical schemes (that are required for accurate LES) require modification for stability, i.e., some type of “limiting” is necessary. Shock capturing options for higher order schemes range from standard limiting approaches to WENO schemes (*e.g.*, Ref. [8]). An alternative approach was used in this study. In order to stabilize the code in the vicinity of strong gradients, such as shock waves, a modification of the classic Jameson, et al. [9] 2-4 dissipation scheme was used. The Jameson's scheme is well validated and used widely with central difference codes to damp out oscillations at shocks. In the original scheme, a fourth order dissipation term was employed to stabilize the central difference scheme in smooth, high cell Reynolds number regions of the flow. In the vicinity of shocks, a pressure based switch was used to deactivate the fourth order dissipation and turn on a second order dissipation term. In the present context, the fourth order dissipation term is not required and is discarded. The second order dissipation term is retained to provide sufficient stability for the fifth order code in the vicinity of shock waves. This new “limiting” scheme is best demonstrated by showing some results for a shock-vortex interaction problem. In this problem a vortex is converted through an oblique shock formed over a wedge. With the limiter, dissipation should only be introduced at the shock and not at the vortex or other regions of the flow, which is critical to ensure the preservation of the vortex. Figure 5(a) shows the contours of vorticity for this problem, while Figure 5(b) shows “pressure-switch” contours, which clearly exhibit that dissipation is added only at the shock and not at the vortex.

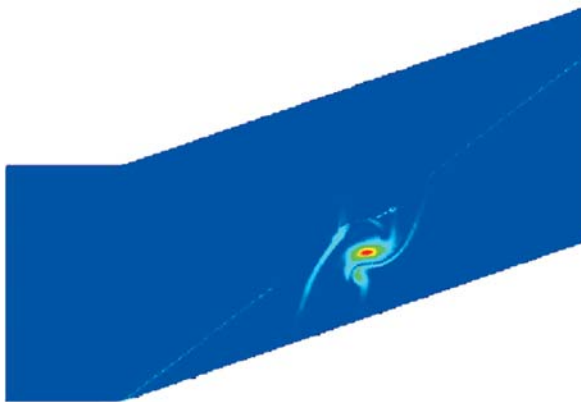


Fig. 5(a). Vorticity contours for shock-vortex interaction test case.

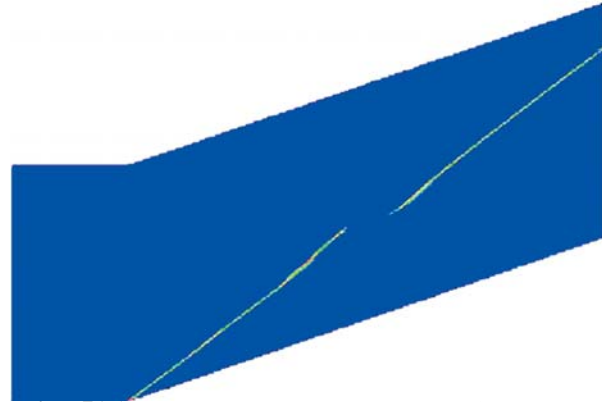


Fig. 5(b). Pressure-switch contours for shock-vortex interaction test case.

The application of this limiting scheme to the lateral divert jet problem is shown in Figure 6. Here the contours of the limiter trigger switch are shown. Again, it is clear that the limiter only acts in shock-like regions and in smooth regions of the flow.

3.2 Study of High-Frequency Control of Cavity Flows

In this section we present results from a study of the mechanism of noise suppression using high frequency actuation. Here, the suppression of cavity tonal and broadband noise by use of a cylinder just upstream of the cavity is studied using a Hybrid RANS-LES method. These simulations are designed to mimic experiments first conducted by McGrath and Shaw [9] in which they used a High Frequency Tone Generator (HFTG) to provide actuation for control of cavity noise. In these experiments, they observed large levels (up to 30dB) of reduction in tonal loads on the floor of the cavity as well as overall suppression of broadband noise levels. A second series of results presented by

Stanek [10] also showed the same trends. While the high frequency turbulence attenuation has been put forth as the explanation of these observations, no complete explanation of the mechanism has been put forth – this study seeks to address this issue.

The flow field simulated here corresponds to the flow field studied experimentally in [11]. The free stream Mach number is 0.6, the cavity has a L/D ratio of 5.6 and the Reynolds number per unit length is 1.45×10^7 . The cavity width to depth ratio is 1.0. The geometry studied here is representative of a 1/72'nd scale model of a F-111 fighter aircraft. The computational mesh for the three dimensional cases consists of approximately 1.375 million points. Details of the simulations and configurations studied are presented elsewhere [12], only an overview is presented here.

The numerical method presented in the previous section is used in the present work is the same as that described in the previous section. The turbulence modeling used in the present work is the Hybrid RANS-LES model developed at CRAFT Tech over the last few years [13].

The contours of the mean velocity for the baseline and controlled cases are shown in Figures 5(a) and 5(b). For the baseline case it is clear that the cavity now behaves more in accord with expectations – the shear layer formed by the separation of the upstream boundary layer jumps over the cavity impinging on the aft end of the cavity. A single large recirculation bubble is formed in the cavity, with small secondary recirculation zones in the corners. From the figure for the controlled case, the effect of the cylinder becomes clear. The shear layer formed over the cavity is now lifted up such that the primary impingement region is no longer the aft wall of the cavity – the shear layer now clears the cavity completely. Thus it is to be expected that the loads on the aft wall are substantially lower. The lifting of the shear layer itself appears to be driven by the flow in the gap between the cylinder and the upstream wall. As can be seen from the figure, a very strong acceleration is seen in that gap, resulting in an asymmetric shedding pattern in the wake of the cylinder. The resulting wake of the cylinder is lifted upwards and the shear layer over the cavity is now primarily formed by this accelerating stream and the free stream. Further, the recirculation region in this case is also seen to be smaller and shifted further downstream such that, near dead flow region is formed near the fore end of the cavity. This contributes to further reduced loads over the fore end of the cavity.

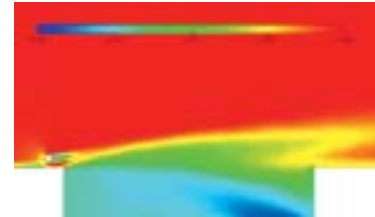
The predictions of the dynamic loads for the baseline and the controlled cases are shown in Figure 5(c). From this plot the preceding discussion becomes clearer – firstly, the dynamic load for the baseline case shows the classic “open” cavity type of behavior. Secondly, the drop in the pressure loading on the aft wall with the introduction of control is clearly visible – the loads on the rest of the cavity floor are also reduced considerably, agreeing with the trend in the behavior of the recirculating region.

In order to understand the reason for the very strong influence of the wire over the cavity flow, it is helpful to understand the effect the wire has on the shear layer. To illustrate this, we plot the iso-surface of vorticity in the shear layer for two cases in Figure 6. Here, the effect of the wire on the instantaneous flow field is seen clearly. In the baseline case, a great degree of coherence is seen in the shear layer. The separated boundary layer rolls up and the structures are strongly two dimensional in nature. Only close to the side-walls of the cavity do we see any evidence of three dimensionality. In the controlled case, however, the flow field even very close to the cylinder is completely three dimensional. The shedding behind the cylinder loses its coherence almost immediately and the strong effect of the longitudinal rollers is seen to tear up the wake region. Very little coherence is left in the flow field. While a full discussion of the effect of the controller is beyond the scope of this paper, the principal differences between the controlled and uncontrolled cases are summarized below. Full details are given in [14] and the reader is referred to that paper for an in depth discussion.

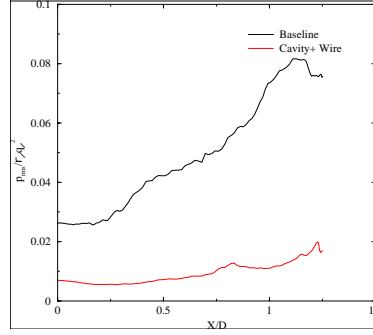
1. The shear layer over the cavity is lofted such that the impingement on the aft end is attenuated.
2. The shear layer is spread out over a wider extent as compared to the baseline case and causes the peak intensity of turbulent stresses in the shear layer to occur farther away from the cavity edge.
3. The magnitude of the peak intensity of the turbulent shear stresses is lower in the controlled case than the baseline case.
4. The integrated turbulent kinetic energy in the shear layer for the controlled case is still higher than the baseline case.
5. Reduced gradients in turbulent shear stresses results in acoustic source strength being attenuated compared to the baseline case.



(a). Baseline case

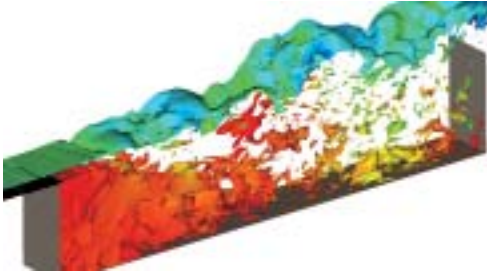


(b). Controlled case.

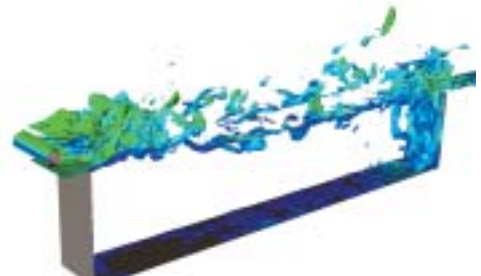


(c). Dynamic loads for baseline and controlled cases.

Fig. 5. Plot of the dynamic loads on the floor of the cavity.



(a). Baseline case.



(b). Controlled case.

Fig. 6. Iso-surface of vorticity (non-dimensional value =1.0) for the baseline and controlled cases.

3.3 Lateral Divert Jet Study

A lateral divert jet flowfield is highly complex involving the interaction of a turbulent boundary layer with a jet. There are shocks, expansions, separation and reattachment phenomena that need to be resolved. Further, a fully developed turbulent boundary layer with the same boundary layer thickness and momentum thickness as the experiment needs to be simulated in order to accurately model the separation/recirculation bubble. A stronger boundary layer will reduce the recirculation bubble while a weaker one will increase it. Over the past year CRAFT Tech personnel have been involved in modeling this type of flowfield caused by the firing of a high pressure ratio jet into a supersonic freestream. The goal of the effort is to predict the unsteady loads on the surface in the separation region.

The domain is $(L_x, L_y, L_z) = (41.2, 15.0, 1.925)d_{in}$ in size and uses $400 \times 250 \times 56$ points in the streamwise, wall-normal and spanwise directions respectively. The inlet is sufficiently far enough that any separation/recirculation bubble ahead of the jet does not affect it. 200 of the 250 points in the wall-normal direction are packed in $3.5 d_{in}$ from the wall to resolve the jet dynamics. The simulation parameters chosen are $U_\infty = 652.5 \text{ m/s}$ ($M_\infty = 3.5$), $T_\infty = 86.5 \text{ K}$, $\rho_\infty = 0.1266 \text{ kg/m}^3$

Contours of temperature along with surface pressures at the corresponding times are shown below at four time intervals. As the jet penetrates the boundary layer, the recirculation bubble advances upstream giving rise to an advancing separation shock. The structure of the recirculation bubble itself is seen to be very unsteady and turbulent and is composed of various small scale vortical structures that cause a highly fluctuating dynamic loading on the wall. The forward moving separation shock in turn also reacts with the shear layer of the divert jet causing a very highly

unsteady flow structure above the Mach disk. The pressure signatures from these structures are analyzed to determine the dynamic loading characteristics on the flat plate.

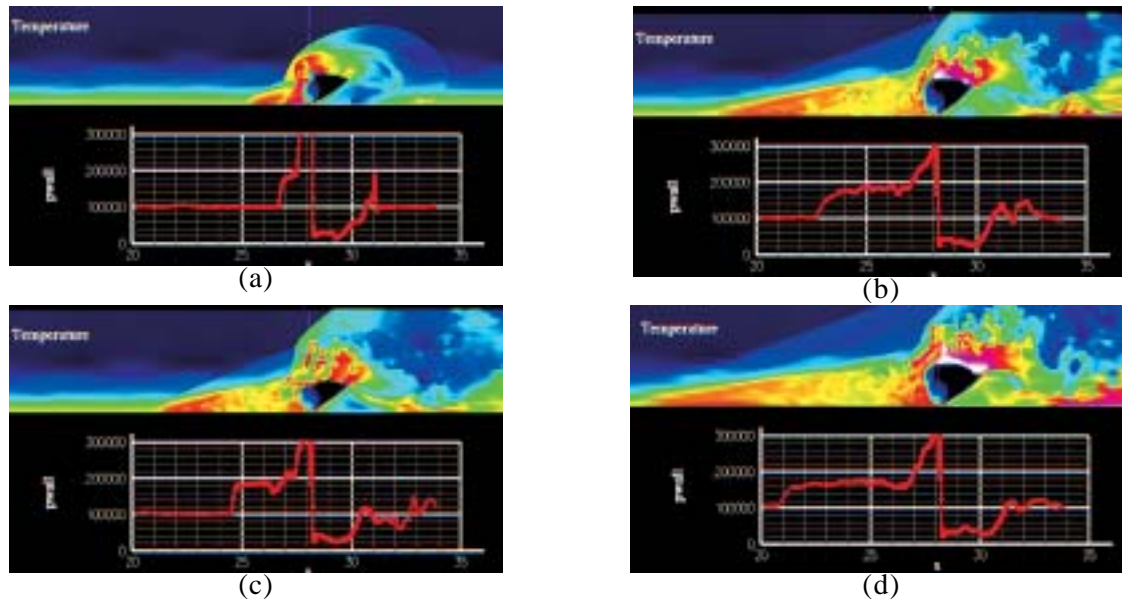


Fig. 6. Temperature contours and surface pressure distributions at four time instances for the lateral jet flowfield.

A more detailed discussion of the physics and numerical issues are presented in [15] and the reader is referred to that paper for details

4.0 MULTI-PHASE GAS/LIQUID METHODOLOGY

An overview of a sophisticated numerical framework designed to perform end-to-end numerical simulations of the dynamic deformation and breakup of bulk liquids interacting with surrounding gas flow is given here (see Refs. 16,17 for details). The framework is geared towards engineering applications and a mixed approach blending first-principles and modeling is used to account for all the major physical phenomena of the problem. The gas/liquid interaction problem is divided into resolvable and non-resolvable scales. The deformation of the liquid bulk is fully resolved using a low-diffusion interface capturing scheme. Phenomena at the gas/liquid interface, including surface tension and primary breakup are modeled and a novel approach developed to simulate primary breakup is presented. The motion of the droplets formed is tracked using fully-coupled Lagrangian and Eulerian solvers. The application of such a framework is suitable for high speed interactions of liquid mass with the atmosphere as would occur when a missile carrying a toxic payload is intercepted but the payload gets released in the atmosphere. The ensuing breakup of the liquid payload and the drop sizes that result are of tremendous interest in determining the region over which the effects of the liquid may be experienced.

The dynamic breakup framework is demonstrated on the problem of a free-flying cylindrical pellet of fluid that is unit problem addressing the liquid dispersion problem discussed above. Initially, a cylindrical pellet is impulsively started at $M = 2$ from right to left, in still air. We first present results for the liquid deformation without droplet formation in Figure 7. As a result of gas/liquid interaction, pressure builds up in front of the drop and the pellet starts to deform, as shown at $t = 0.4$ (ms). The front shoulder of the blob starts rolling back and liquid is pulled out of the back. Later in time, at $t = 2.4$ (μ m), the liquid carried from the shoulder and the back reflect off of the centerline and spread outward, away from the blob, and inwards, towards the back side of the pellet.

We next present results with droplet generation in Figures 8 and 9. As can be seen from the contours of liquid mass fraction in Figure 8, the changes are very drastic. The large roll-ups observed in Fig. 7 are now absent and vigorous mass shedding takes place at the shoulder and the back of the pellet, where the shear is highest. Droplet cloud densities shown in Figure 9 indicate very high densities are observed near the drop shoulder and the back of the drop, in qualitative accord with photographs of shock wave / drop interactions in shock tubes. The drop size distributions are also in qualitative accord with experimental observations of drop shattering. The smaller drops, which equilibrate fastest with the slower moving gas, are found on the outer edges of the cloud and the

larger drops are close to the pellet. These calculations illustrate the ability of the gas/liquid framework to model gas/bulk liquid interactions as part of an interface capturing numerical procedure with a coupled dense spray procedure to track the droplets that are generated at the dynamically evolving liquid interface.

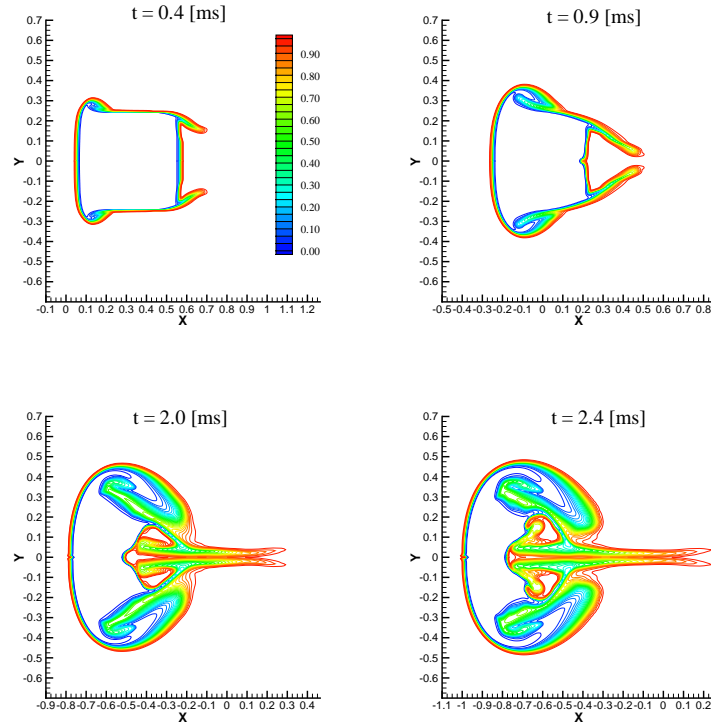
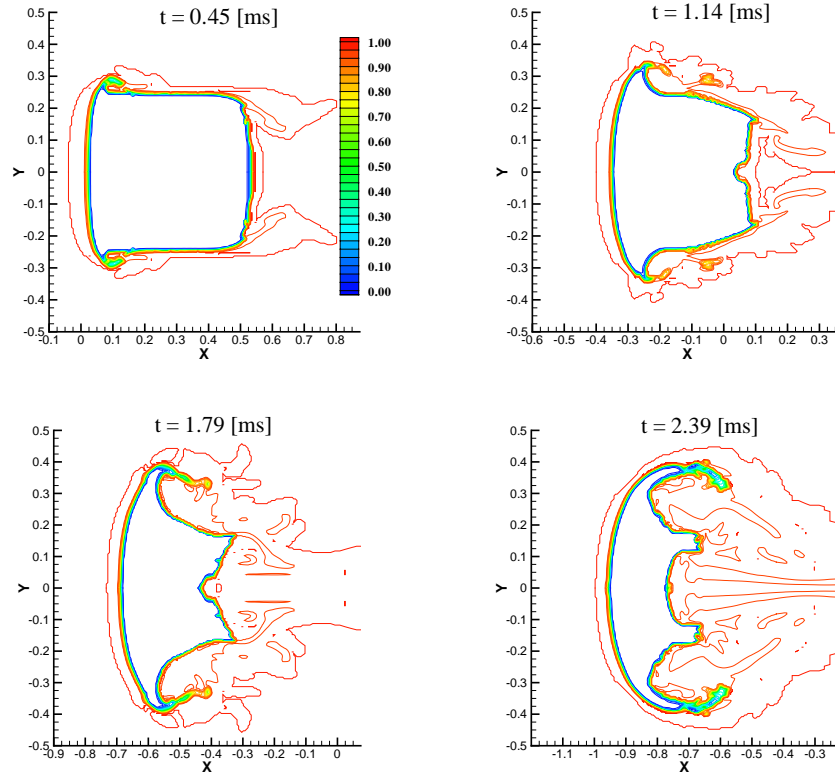


Fig. 7. Free flight of a cylindrical pellet of fluid. Contours of gas mass fraction.



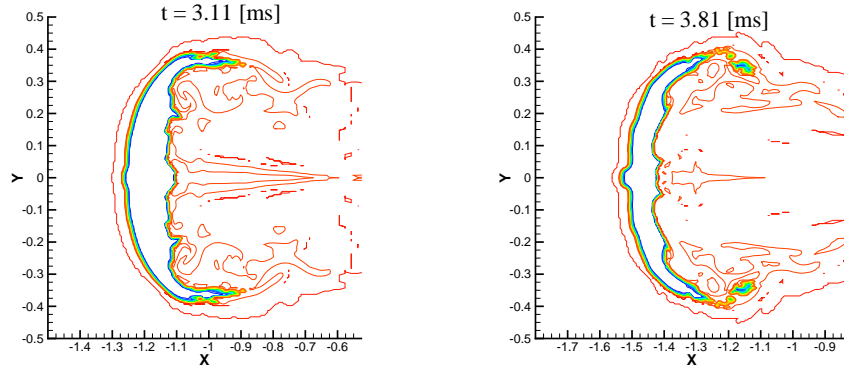


Fig. 8: Free flight of a cylindrical pellet of fluid. Breakup without tracking of the broken mass. Contours of gas mass fraction.

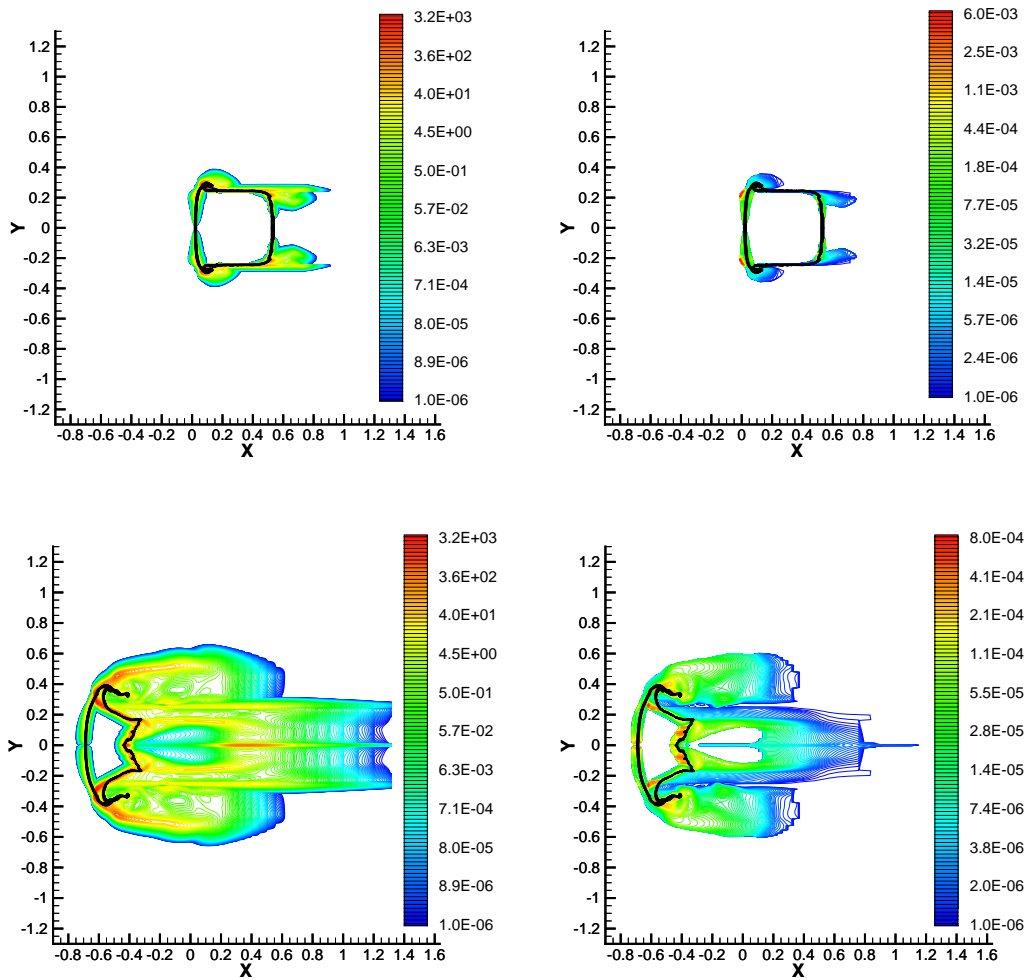


Fig. 9. Free flight of a cylindrical pellet of fluid. Breakup with Eulerian tracking of the particulate continuum. Contours of gas mass fraction (black) superimposed on top of contours of particulate cloud density (color, left) and contours of cloud SMD (right, color).

5.0 REFERENCES

- [1] Hosangadi, A., Lee, R.A., Cavallo, P.A., Sinha, N., and York, B.J., "Hybrid, Viscous, Unstructured Mesh Solver for Propulsive Applications," AIAA Paper 98-3153, 34th Joint Propulsion Conference, Cleveland, OH, July 13-15, 1998.

- [2] Cavallo, P.A., and Baker, T.J., "Efficient Delaunay-Based Solution Adaptation for Three-Dimensional Unstructured Meshes," AIAA Paper 2000-0809, 38th Aerospace Sciences Meeting and Exhibit, Reno, NV, January 10-13, 2000.
- [3] Baker, T.J., and Cavallo, P.A., "Dynamic Adaptation for Deforming Tetrahedral Meshes," AIAA Paper 99-3253, 14th Computational Fluid Dynamics Conference, Norfolk, VA, June 28-July 1, 1999.
- [4] Cavallo, P.A., Hosangadi, A., Lee, R.A., and Dash, S.M., "Dynamic Unstructured Grid Methodology with Application to Aero/Propulsive Flowfields," AIAA Paper 97-2310, 15th Applied Aerodynamics Conference, Atlanta, GA, June 23-25, 1997.
- [5] Baker, T.J., "Deformation and Quality Measures for Tetrahedral Meshes," European Congress on Computational Methods in Applied Science and Engineering, ECCOMAS 2000, Barcelona, Spain, September 2000.
- [6] Cavallo, P.A., and Dash, S.M., "Aerodynamics of Multi-Body Separation Using Adaptive Unstructured Grids," AIAA Paper 2000-4407, 18th Applied Aerodynamics Conference, Denver, CO, August 14-17, 2000.
- [7] Karypis, G., Schloegel, K., and Kumar, V., "ParMETIS: Parallel Graph Partitioning and Sparse Matrix Ordering Library," Technical Report, University of Minnesota, Department of Computer Science and Engineering, 1997.
- [8] Liu, X. D., Osher, S., and Chan, T., "Weighted essentially non-oscillatory schemes", Journal of computational physics, Vol. 115, pp 202-212, 1994.
- [9] Jameson, A., Schidt, W., and Turkel, E., "Numerical solutions of the Euler equations by finite-volume methods using Runge-Kutta time-stepping schemes, AIAA paper 81-1259, Jun 1981.
- [10] McGrath, S. and Shaw, L.L., "Active Control of Shallow Cavity Acoustic Resonance, " AIAA 96-1949, 1996.
- [11] Stanek, M.J., Raman, G., Kibens, V., Ross, J.A., Odedra, J. and Peto, J.W., "Control of Cavity Resonance Through Very High Frequency Forcing," AIAA 00-1905, 2000.
- [12] Sinha, N. and Arunajatesan, S., and Ukeiley, L., "High Fidelity Simulation Of Weapons Bay Aeroacoustics Attenuation Using Active Flow Control," Paper No. AIAA-2000-1968, 6th AIAA/CEAS Aeroacoustics Conference, Lahaina, Hawaii, June 12-14, 2000.
- [13] Arunajatesan, S.A., Shipman, J., and Sinha, N., "Hybrid RANS-LES Simulation of Cavity Flowfields with Control," AIAA Paper No. 1130, 40th AIAA Aerospace Sciences Meeting and Exhibit, Reno, NV, January 14-17, 2002.
- [14] Arunajatesan, S.A. and Sinha, N., "Unified Unsteady RANS-LES Simulations of Cavity Flowfields," AIAA Paper No. 2001-0516, 39th AIAA Aerospace Sciences Meeting and Exhibit, Reno, NV, January 8-11, 2001.
- [15] Kannepalli, C., Arunajatesan, S., and Dash, S.M., "RANS/LES Methodology For Supersonic Transverse Jet Interactions with Approach Flow," AIAA Paper No. 1139, 40th AIAA Aerospace Sciences Meeting and Exhibit, Reno, NV, January 14-17, 2002.
- [16] Hosangadi, A., Sinha, N., and Dash, S.M., "A Unified Hyperbolic Interface Capturing Scheme for Gas/Liquid Flows," AIAA-97-2081, 13th AIAA CFD Conferences, Snowmass, CO, June 29-July 2, 1997.
- [17] Tonello, N.A., Dash, S.M., and Perrell, E.R., "Advanced Computational Framework For Dynamic Bulk-Liquid Gas Interactions," AIAA Paper-99-2205, 35th AIAA/ASME/ SAE/ASEE Joint Propulsion Conference and Exhibit, Los Angeles, CA, June 20-24, 1999.